

# 用于多比特量子存储器的低温离子阱系统

**Cryogenic Trapped-Ion System for  
Multiqubit Quantum Memory**

(申请清华大学工学硕士学位论文)

培养单位：计算机科学与技术系

学 科：计算机科学与技术

研 究 生：薛 瑞 尼

指 导 教 师：郑 纬 民 教 授

副指导教师：陈 文 光 教 授

二〇二三年三月



# **Cryogenic Trapped-Ion System for Multiqubit Quantum Memory**

Thesis submitted to  
**Tsinghua University**  
in partial fulfillment of the requirement  
for the degree of  
**Master of Science**  
in  
**Computer Science and Technology**

by  
**Xue Ruini**  
Thesis Supervisor: Professor Zheng Weimin  
Associate Supervisor: Professor Chen Wenguang

**March, 2023**



# 关于学位论文使用授权的说明

本人完全了解清华大学有关保留、使用学位论文的规定，即：

清华大学拥有在著作权法规定范围内学位论文的使用权，其中包括：（1）已获学位的研究生必须按学校规定提交学位论文，学校可以采用影印、缩印或其他复制手段保存研究生上交的学位论文；（2）为教学和科研目的，学校可以将公开的学位论文作为资料在图书馆、资料室等场所供校内师生阅读，或在校园网上供校内师生浏览部分内容；（3）按照上级教育主管部门督导、抽查等要求，报送相应的学位论文。

本人保证遵守上述规定。

作者签名：\_\_\_\_\_

导师签名：\_\_\_\_\_

日 期：\_\_\_\_\_

日 期：\_\_\_\_\_



## CHAPTER 1 NOTATION

$^{171}\text{Yb}^+$

## CHAPTER 2 EXPERIMENTAL SETUP

The rate of background gas collisions with the ion chain is one of the scaling challenges in an ion-trapped system. Such collisions may destroy the qubit's information and result in the loss of the whole chain. Thus, it is essential to construct an extreme high vacuum (XHV) environment to reduce the vacuum system's background gas pressure.

### 2.1 The cryostat

The cryostat is the key equipment of the cryogenic trapped ion system. We need to pay attention to some key technical indicators when choosing the model of the cryostat, designing the internal support structure and the assembly structure of the trap-related components. The most critical technical indicators are cooling capacity and vibration. Low temperature is the advantage of the cryogenic trap over the room-temperature trap. We can achieve low pressure by cryo-pumping to reduce the collision rate of trapped ions with residual background gas, thereby increasing the lifetime of trapped ions. The price of cryo-pumping is additional vibration, however, the vibration can be reduced to a degree that does not affect quantum gate fidelity. In experiments, we often use these two parameters to characterize the cooling capacity. One is the lowest temperature that the system can reach when the cryogenic trap is not temperature stabilized, and the other is the heating power at the sample mount when the temperature of the cryogenic trap is stabilized above the liquid helium temperature zone and the vibration caused by liquid helium is reduced to a certain range. Another key technical indicator of the cryostat is the long-term stability at the sample, including changes in displacement and background electric field. This will affect the calibration period of the ion trap experiment. Calibration that is too frequent indicates a lack of robustness in the experiment system.

There are several different types of cryostats on the market. One of these is the flow cryostat, which has lower cryocooler vibration noise but requires constant replenishment of cold liquid coolant, which is expensive and time-consuming. In contrast, the cryogenic trapped ion system in our lab uses a closed-loop Gifford-McMahon cryostat. This type of cryostat uses closed-cycle helium gas as operation material in cooling cycle and does not require constant refilling of the coolant. It is very convenient to use and cheap to maintain as it only needs external electric supply. One of the advantages of this closed-loop cryostat

---

## CHAPTER 2 EXPERIMENTAL SETUP

---

is that it has a vibration isolation system (VIS). The vibrating cold finger is mechanically separated from the main vacuum by a helium-filled exchange gas region at a pressure 0.03 bar above atmospheric. The vibration isolation system is the only mechanical coupling between the cold head and the main vacuum apparatus which is mounted on an optical breadboard. In the vibration isolation system region, it is sealed with a helium-confined rubber bellows. The helium gas serves as the thermal link between the cold finger and the sample mount where the ion trap is mounted. Another advantage of this closed-cycle cryostat is that its structure is relatively simple, and we can increase cooling capacity and reduce vibration through optimized design, because it is difficult to optimize each parameter independently in a complex system.

Table 2.1 Refrigeration capacity (typical).

	RDK-408D2	RDK-415D2
First stage	40 Watts @ 43 (50Hz)	35 Watts @ 50K (50Hz)
	50 Watts @ 43 (60Hz)	45 Watts @ 50K (60Hz)
Second stage	1.0 Watt @ 4.2K (50/60Hz)	1.5 Watt @ 4.2K (50/60Hz)

The cryostat is model SHI-4XG-15-UHV, designed and manufactured by Janis Inc. In order to reduce vibration, we provide some design suggestions. The cryostat consists of a cold head, an exchange gas space and a vacuum chamber. The cold head is powered by a helium compressor. The models of cold head and helium compressor are RDK-415D2 and F70-H produced by Sumitomo Corporation of Japan. The cold head features two stages with different refrigeration capacity: the 40 K stage has  $\sim 35$  W, and the 4 K stage has 1.5 W, as shown in Table 2.1. The cold head must be fixed near the vacuum chamber, but there are only three interfaces of the cold head: the power supply, the supply high-pressure helium tube and the return high-pressure helium tube. Therefore, we placed the helium compressor and water cooler in the grey room of the laboratory to further isolate the source of vibration noise. The single continuous running time of the cold head can exceed 10,000 hours, which is enough for us to carry out long-term experiments.

The exchange gas space, as shown in Fig 2.1, is mainly composed of rubber bellow, helium pressure gauge and some helium valves, the top and bottom are respectively connected to the cold head and the vacuum chamber. The role of bellow is to reduce the vibration generated by the cold head and directly transmitted to the vacuum chamber, because rubber is more elastic than stainless steel. I think it is worth trying to replace the rubber bellow with a stainless-steel sheet that has been bent many times, because using

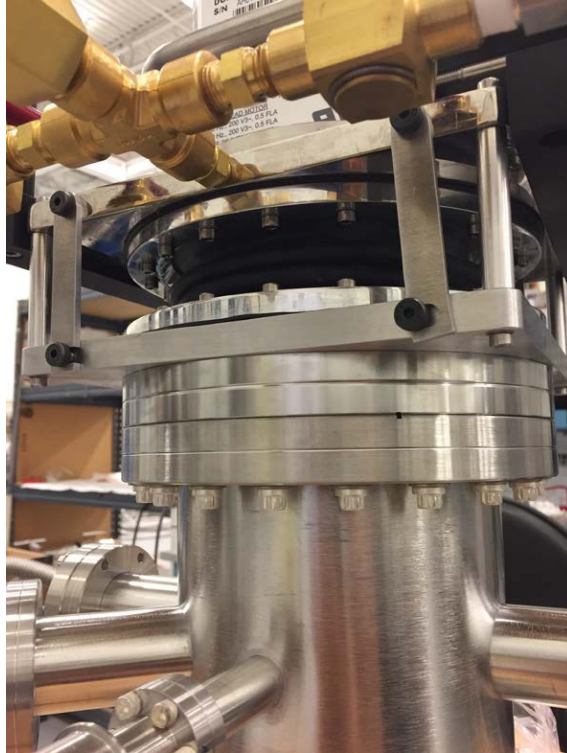


Figure 2.1 Exchange gas space.

a rubber bellow may cause leakage in the long-term operation of the system. Leakage of rubber bellow may come from three aspects. Firstly, the rubber material will deteriorate after a long-time use, our system has a leakage problem after about 2 years of operation, which is manifested as water inside the exchange gas space after the process of cooling down and warming up. Secondly, the rubber bellow is prone to defects during machining, we contacted our supplier to process a new rubber bellow after we found the leakage problem, and found that some of the rubber bellow had defects on the surface during many attempts. Finally, the sealing method of rubber bellow is worse than that of stainless steel, our cryostat uses o-ring to seal rubber bellow. We tried to have the supplier process different rubber bellow to test the leakage, such as testing different materials and thickness of rubber bellow, in some poor cases after a single cooling and reheating process will appear leakage, we finally used silicone rubber bellow and the thickness is twice the original and no leakage has been found so far.

## 2.2 Cryogenic and UHV system

The vacuum chamber resembles a cylinder with a diameter of about 200 mm and a height of about 600 mm. Externally, the upper part of the vacuum chamber has some

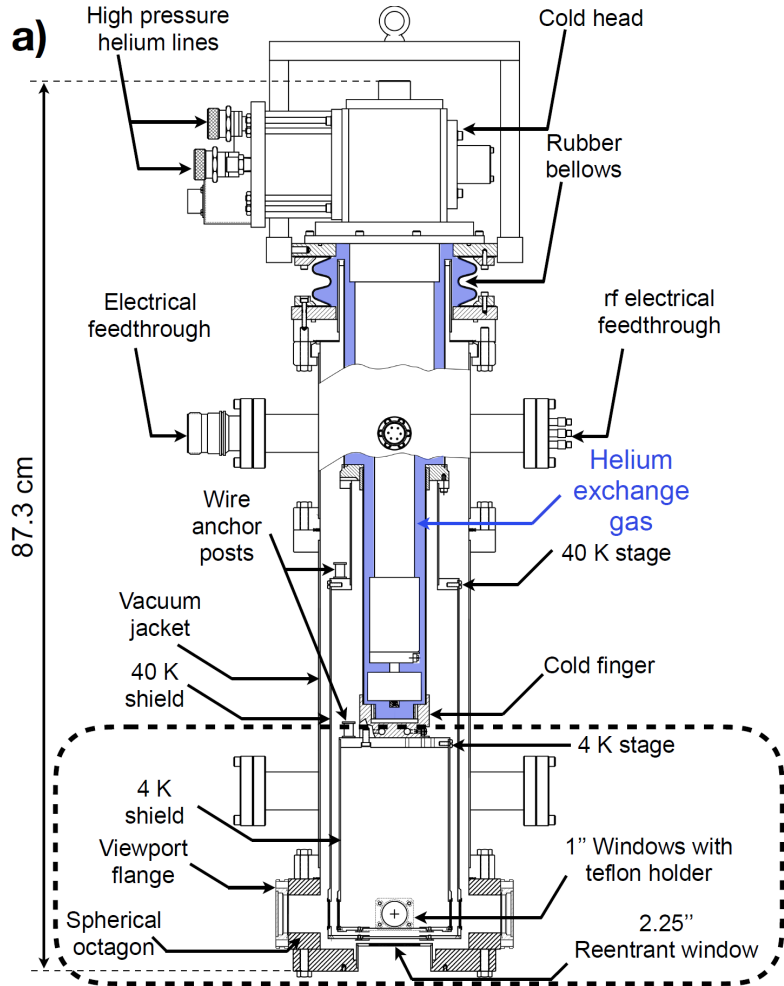


Figure 2.2 The side section view of the Gilford-McMahon cryostat.

feedthroughs connecting the electrical equipment to the vacuum equipment, and the lower part is a spherical octagon. The top of the vacuum chamber is in contact with the exchange gas space, and the bottom is the re-entrant window. In our experiments, we used a total of three electrical feedthroughs, one DC feedthrough to drive the voltage signal to the electrodes of the trap, another DC feedthrough to drive the thermometer and heater in the vacuum chamber, and an RF feedthrough to drive the RF signal to the resonator. Below them, there are a total of three Vacuum feedthroughs, one connected to an ion gauge (Agilent UHV-24P) to monitor the vacuum level in the vacuum chamber, one connected to a NEG-Ion pump (SAES NextTorr Z100) to pump out hydrogen, since hydrogen is the least efficiently cryo-pumped gas, and an angle valve to pump out vacuum during system maintenance. A spherical octagon holds eight 1" diameter windows to provide optical access in the horizontal plane, the windows are made of UVFS and have different wavelength optical coatings according to the optical path design. We replaced one of the windows along the trap axis with an oven feedthrough, and installed both enriched

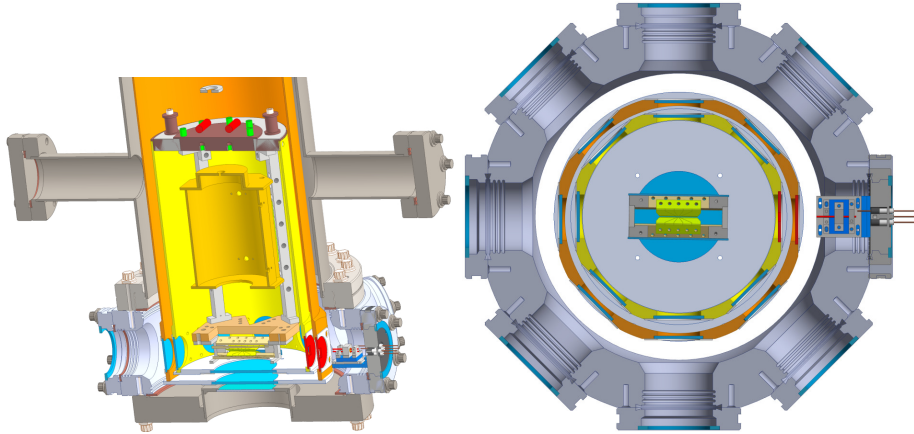
$^{171}\text{Yb}$  oven and enriched  $^{174}\text{Yb}$  oven on it, and finally tested them to work. However, assembly errors during installation may cause the Yb flux cannot enter the trap during ion loading, we can increase the translation degrees of freedom when designing the part to solve this problem. According to our experience, because of the large divergence angle of Yb flux, we just need to be able to see the trap and oven through the opposite window. The re-entrant window located at the bottom of the vacuum chamber has a diameter of 2.25", below which is the imaging system. The maximum numerical aperture allowed for imaging ions along the vertical direction is 0.5. The Re-entrant window is surrounded by a doughnut-shaped aluminum base placed on an optical breadboard, and the base carries the full weight of the vacuum chamber. We tried to fasten between the upper part of the vacuum chamber and the optical breadboard with an aluminum sloped beam, but it did not reduce the vibration of the trap, indicating that the current support structure is solid enough.

Table 2.2 Table of electrical devices connected to the vacuum chamber.

Device	Model
ion gauge	Agilent UHV-24P
NEG-Ion pump	AES NextTorr Z100
DC signal source	Homemade 16-channel AD5791
RF signal source	Rohde & Schwarz SMB-100B

The main components inside the vacuum chamber are the 40 K shield, the 4 K shield and the sample mount. These two shields are used to shield the ion trap from room temperature blackbody radiation, their material is aluminum, but copper may be a better choice because copper material has a higher thermal conductivity. The bottom of the two shields are eight 1" UVFS windows, which correspond to the spherical octagon and have the same optical coating. The glass is fixed in the groove by the Teflon holder in order to keep the windows from being crushed during the cooling procedure, however, because of the elasticity of Teflon, the positioning accuracy of the windows is poor, which may be the main source of optical aberration. The top of the 40 K shield is in contact with the 40 K stage of the cold head through the helium gas in the exchange gas space, which is usually higher than 40 K, we named it that way just because it is intuitive. The top of the 4 K shield is fixed to the sample mount, which is made of oxygen-free copper with a gold-plated surface to obtain a high thermal conductivity and to prevent oxidation during system maintenance. The sample mount and the 4 K stage of the cold head are separated

by a heat exchanger and cryogenic helium gas. The 4 K stage can reach temperatures below 4 K, and the heat exchanger is composed of a series of concentric circular oxygen-free copper sheets, which are designed to increase the cooling capacity at the sample mount. However, if the position between a pair of heat exchangers is shifted during operation and touches each other, it can introduce large vibrations to the sample mount, for example when floating the optical table.



(a) The oblique view of ion trap and (b) The top view of ion trap and vacuum chamber.

Figure 2.3 The design and related information of the cryostat.

Although the refrigeration capacity of the 4 K stage in the cold head reaches 1.5 W, the cooling capacity of the sample mount in the vacuum chamber, which is directly available to the user, is much lower. The reduction of the cooling capacity comes from the heat conduction between the 4 K stage and the sample mount and the heat leakage from the environment. In order to improve the heat transfer between the 4 K stage and the sample mount, we can increase the surface area of the heat exchanger, we can also fill the exchange gas space with sufficient helium gas, and it is necessary to use oxygen-free copper to produce thermally conductive parts. In our experiments, we use auto gas charging system to stabilize the helium pressure in the exchange gas space at a fixed positive pressure. It is worth noting that the rubber bellow loses its vibration isolation function under negative pressure, and the life of the rubber bellow is reduced. The auto gas charging system was designed by PHYSIK and is based on the principle of using a PLC to read the helium pressure gauge and control the opening and closing moments of the helium valves, which will eventually stabilize the helium pressure gauge at 1.03 bar. There are two helium valves to control the helium inlet and outlet, and one safety valve to allow excess helium to escape, preventing the bellow from bursting when the auto gas charging

system is not working. The temperature stabilize system is a kit we purchased from Janis Inc. and consists of a thermometer, heater and temperature controller. The thermometer (DT-670-CU-HT-1.4H) is located inside the sample mount in the vacuum chamber and has a measurement range of 1.4-500 K, covering the cryostat operating range of approximately 4-300 K. The heater is a  $25 \Omega$  resistor very close to the thermometer. The DC lines of the heater and the thermometer are connected to the temperature controller (Model 26 from CryoCon) on the instrument rack via a DC feedthrough on the vacuum chamber. In low temperature operation, the temperature of the sample mount can be stabilized at  $6 \pm 0.05$  K for a long time by setting the appropriate PID parameters, as shown in Fig 2.4. The output power of the heater is about 350 mW, which means that the refrigeration capacity of the sample mount has a margin of 350 mW.

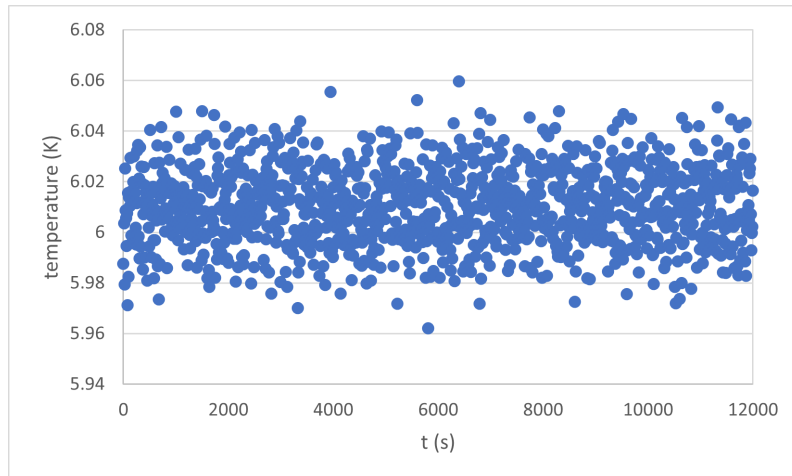


Figure 2.4 The stablized temperature of the sample mount.

The auto gas charging system and the temperature stabilize system are the key systems for the long-term stability of the cryostat. Although the temperature of This cryostat has almost no drift, we can observe that the trap can shift  $\pm 1 \mu\text{m}$  during the experiment. The operation to avoid the effects of such position shifts by frequent calibration of the system parameters is very complicated, so this instability can be fatal for an experimental system. The long drift of the sample mount comes from the mechanical structure of the cryostat. The auto gas charging system can only stabilize the helium pressure near the rubber bellow, and the 40 K stage and 4 K stage of the cold head are not stabilized. Therefore, the pressure and temperature in the contact part of the vacuum chamber and the exchange gas space cannot be stabilized for a long time. However, this part is the support point of the sample mount, so the sample mount will be disturbed by these external environmental changes. We can consider fixing the sample mount to the room temperature

area of the vacuum chamber, which will not move if the laboratory environment is stable, but this will inevitably increase the heat leakage from the room temperature area. In our experiments, we first pumped the vacuum chamber to  $1 \times 10^{-6}$  mbar at room temperature using the Turbo Pump, then activated the NEG-Ion Pump for about 2 hours, and at the end of the operation the vacuum chamber vacuum level dropped to  $1 \times 10^{-8}$  mbar. The vacuum chamber can reach a vacuum level of  $3 \times 10^{-10}$  mbar with the effect of the cryo-pump.

## 2.3 Helical resonator and segmented blade trap

The blade trap forms a capacitor of approximately 6 pF. In order to drive this capacitor, i.e. to apply a high voltage signal to it, we need a larger helical resonator to form the LC oscillation circuit and to achieve impedance matching. The two components are therefore closely linked. The helical resonator and the blade trap are both located inside the 4 K shield of the vacuum chamber. The helical resonator is fixed underneath the sample mount and then the blade trap is fixed underneath the helical resonator. This ensures that the helical resonator and the blade trap are very close to each other and that their temperatures are equally stable. At the same time the low temperature allows the resistance in the oscillator circuit to be significantly reduced, which helps to increase the quality factor of the oscillator circuit. The helical resonator and the blade trap are used as a single unit and its input and output are achieved via RF and DC electric feedthrough.

### 2.3.1 Design of helical resonator

The circuit models for the helical resonator and the blade trap have been well studied. In practice, we have developed a very mature design procedure with a high quality factor, choosing only two parameters  $b/d$  and  $d/D$  to optimise the performance of the helical resonator with the quality factor as the objective function. We can calculate the loading frequency in the empirical parameter regime using the trap capacitance and the quality factor. Typically,  $b/d \approx 1.5$  and  $d/D \approx 0.5$  is a good choice, and if the loading frequency meets our requirements we will try to choose the highest quality factor around this parameter range, as shown in Fig 2.5. A two-wire spiral resonator is much more complex than a single-wire spiral resonator because of the coupling between the two coils. However, for the sake of simplicity we are still using the model and we can achieve an accuracy of about  $\pm 5$  MHz. To ensure that the phase and amplitude of the two coils are the same, we

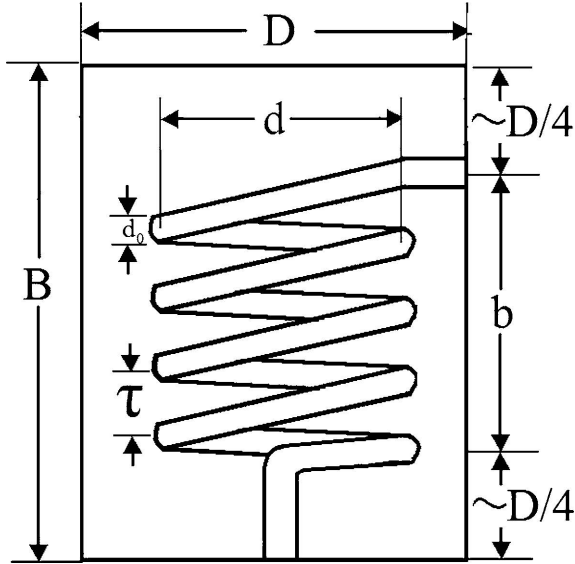
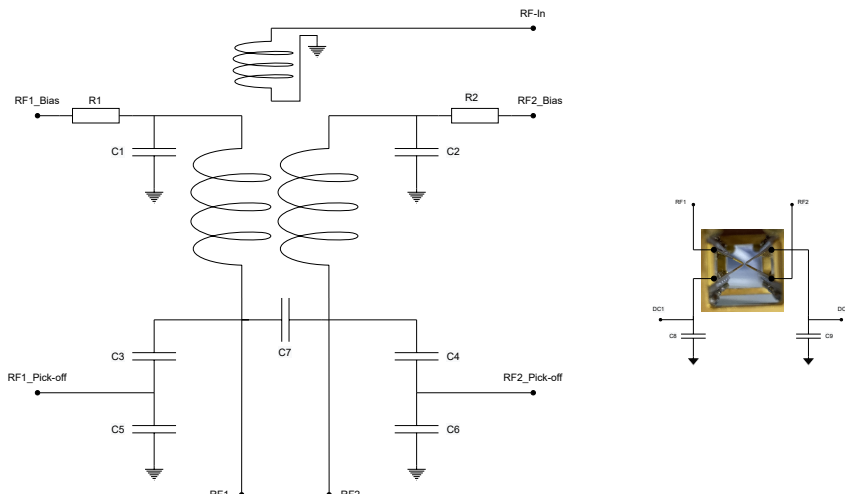


Figure 2.5 The outline design of a helical resonator.

use a parallel capacitor, which is shorted when connected to the RF feedthrough, with a capacitance of approximately 300 nF. The two-wire design is designed to help minimise micro-movements by applying a DC voltage to the RF electrodes, so we need to ensure that the RF signal on the coil is grounded and the DC voltage is not, this is achieved by a 300 nF capacitor connected to the shield. In addition, we added an RC filter before the DC voltage was connected to the coil.

### 2.3.2 Circuit diagrams of the helical resonator and the blade trap



(a) Circuit diagrams of the helical resonator. (b) Circuit diagrams of the blade trap.

Figure 2.6 Circuit diagrams of the helical resonator and the blade trap.

To facilitate our understanding of the circuit structure of the helical resonator and the

blade trap, Fig 2.6(a) shows their equivalent circuit diagrams. In Fig 2.6(b), an external RF signal (RF-In) is fed to a small antenna. The antenna is coupled to a double bifilar helical copper wire, which is short-circuited by a large capacitor (C7, 330nF). The two RF bias signals (RF1 Bias and RF2 Bias) are supplied by the AD5791 and pass through an RC filter consisting of a resistor (R1, R2, 10 kΩ) and a capacitor (C1, C2, 330 nF) to add a DC bias to the respective RF signal. The two capacitively coupled signals (RF1 Pick-off, RF2 Pick-off) can be coupled to a 1% RF resonant signal. The voltage divider circuit uses a small capacitor (C3, C4, 0.2 pF) and a large capacitor (C5, C6, 20 pF) in series. The signal from the two pairs of DC electrodes on the blade trap (DC1, DC2) is grounded through large capacitors (C8, C9, 820 pF).

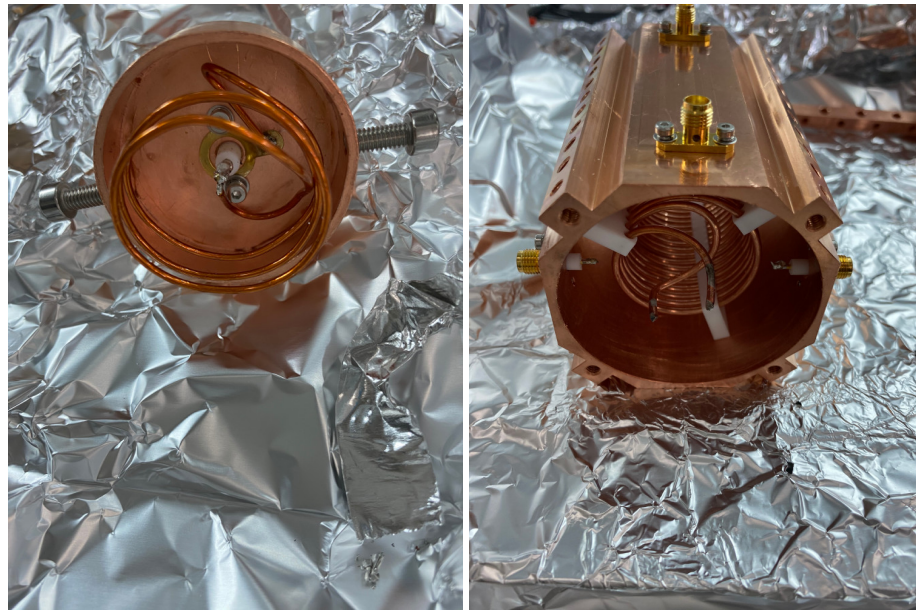
Table 2.3 Table of electronic components in the circuit diagrams.

Component	Value	Model	Parameters
Resistor	10 kΩ	RNCF1206TKY10K0	RES 10K OHM 0.01% 1/4W 1206
Capacitor	0.2 pF	VJ1111D0R2VXRAJ	1.5KV
Capacitor	20 pF	800B200JT500XT	CAP CER 500V C0G/NP0 1111
Capacitor	820 pF	C0805C821JCGACTU	CAP CER 500V C0G/NP0 0805
Capacitor	330 nF	C2220C334J1GACTU	100V NP0

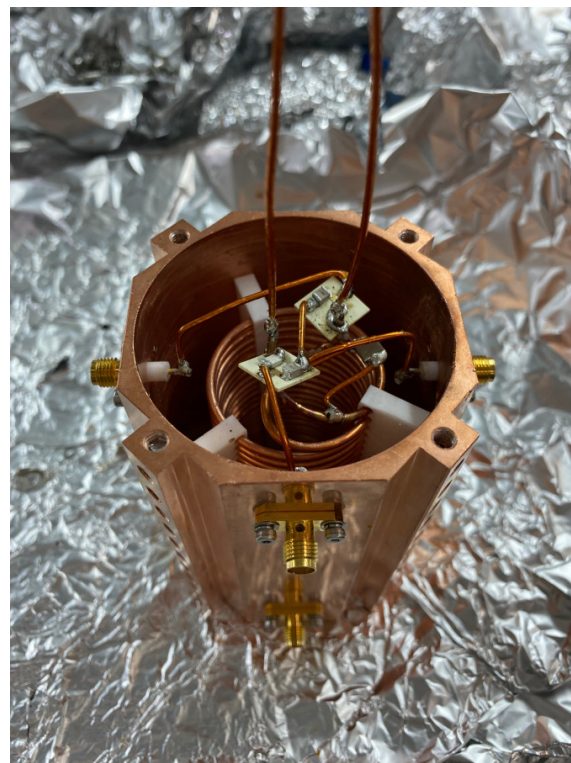
### 2.3.3 Assembly of the helical resonator

The material used for the body of the helical resonator is oxygen-free copper, which is characterised by its very low resistivity and high thermal conductivity. The low resistivity helps to obtain a high quality factor, but the oxygen-free copper is susceptible to oxidation during processing, so the oxide film needs to be removed before assembly. After the helical resonator has been assembled, it needs to be placed in a vacuum enclosure to prevent oxidation.

The main parts of the helical resonator were machined according to the design parameters: the antenna cover, the top cover, the middle part, the bottom cover and the helical coils, which were then cleaned in the ultrasound machine using acetone and ethanol. After drying these parts with nitrogen and soaking them in organic acid for 5 minutes, it can be observed that the surface oxide film disappears and turns purplish red. We soak the parts in plenty of distilled water to remove the residual organic acid and then dry the parts with



(a) Assembly of the helical resonator  
antenna. (b) Assembly of the main section.



(c) Assembly and soldering of the PCB.

Figure 2.7 Assembly of the helical resonator.

Table 2.4 Assembly procedures of the helical resonator.

Procedure	Content
Preservation	Oxygen-free copper components should not be left in the air for long periods of time and need to be placed in a vacuum enclosure.
Clean	<p>Disassemble the helical resonator and take out the oxygen-free copper components individually into large beakers in preparation for sonication.</p> <p>Sonicate them with acetone for 30 minutes and with ethanol for 5 minutes.</p> <p>Blow the components dry.</p> <p>Soak them in organic acid for 5 minutes, where the surface oxide film can be observed to disappear and turn purplish red.</p> <p>Remove residual organic acids from the surface by immerse them in plenty of distilled water.</p> <p>Wipe the surface of the oxygen-free copper components with paper, place them in a vacuum hood and evacuate the vacuum enclosure.</p>
Preparation	<p>Cut a number of thick wires into suitable length and trim off the insulation at both ends.</p> <p>Prepare the PCB, capacitors, resistors, screw coil retainers, SMA connectors, copper plated components, indium foil, screw sets, spanners.</p> <p>Soak the capacitors, resistors and indium foil in acetone for 30 minutes and in ethanol for 5 minutes, sonicate the rest in acetone for 30 minutes and in ethanol for 5 minutes.</p>
Test	<p>Measure the inductance of the helical resonator with an LCR meter. (1.50 <math>\mu</math>H and 1.41 <math>\mu</math>H.)</p> <p>Measure the scattering parameters of the helical resonator with a vector network analyzer.</p> <p>The antenna position and pitch were adjusted to match the impedance when the helical resonator was unloaded. (<math>f = 69.15</math> MHz, <math>Q = 434.7</math> U, <math>R = 50.90</math> dB.)</p> <p>After the helical resonator is connected to the Trap, the antenna position and pitch are adjusted so that the impedance matches, and at this point the RC filter is connected. (<math>f = 36.83</math> MHz, <math>Q = 373.6</math> U, <math>R = 28.05</math> dB.)</p>

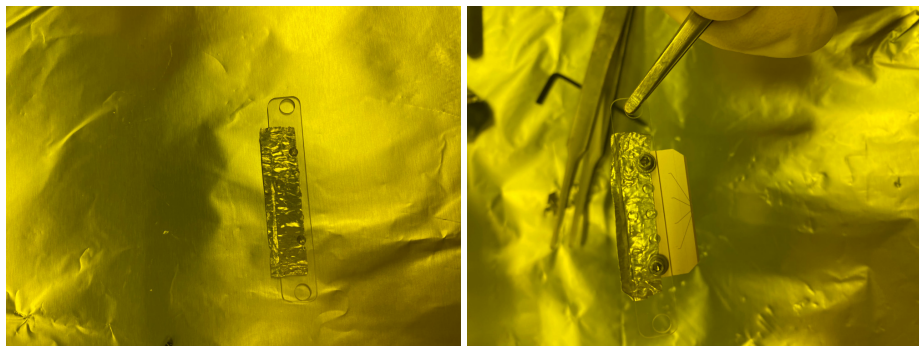
nitrogen. The cleaning of the parts of the main part of the copper tube is now complete. This part needs to be done carefully, as the oxide film on the helical resonator surface affects the quality factor.

We also need to prepare and clean the rest of the parts according to the design parameters to meet the ultra-high vacuum requirements. We then soldered the circuit components together using lead-free solder. The parts are then assembled with stainless steel screws, each requiring a resilient pad to prevent the screws from loosening at low temperatures.

### 2.3.4 Assembly of blade trap

The advantage of the blade trap is that it is easy to process and assemble, but the disadvantage is that the assembly error is higher compared to the surface trap or the monolithic trap, which causes an asymmetry in the electrostatic potential at the centre of the trap where the ions are located, i.e. a deviation from the linear trap configuration. When designing the blade trap for use in the cryostat, we need to take care that the material has a high thermal conductivity and that the connections between the components are sufficiently tight. In this way we can achieve the lowest temperatures on the blade trap. This helps to obtain a higher vacuum level and to extend the life of the ions.

The blade trap consists of four blade-shaped electrodes, one pair of DC electrodes and one pair of RF electrodes. The blade is processed by laser cutting the ceramic substrate and then plating the surface with a gold layer. The electrodes are machined with a certain amount of error and defects on the surface of the electrode closest to the ion produce a high level of electrical noise, which can be reduced by improving the process. We have machined a sapphire adapter plate and mounted the blade on the sapphire adapter plate and then mounted the sapphire adapter plate on an oxygen-free copper holder. We designed this adapter to avoid a short circuit between the blade and the ground (the blade holder). In order to increase the thermal conductivity, we need to cover these contact surfaces with indium foil. For the fixing of the components we used stainless steel screws and used resilient pads on each screw. This is to prevent the screws from loosening during the cooling down process, and to prevent the blade from being crushed by excessive torque when tightening the screws. Once installed we had to fine-tune the position of the sapphire adapter under the microscope to keep the assembly error small enough. This operation makes use of the fact that the diameter of the through-hole is slightly larger than the diameter of the screw. Since the assembly is done by hand, this part of the assembly error is unavoidable.



(a) Assembly of the sapphire and indium film.  
(b) Assembly of the blade.



(c) Assembly of the PCB and the gold ribbon.

Figure 2.8 Assembly of the blade trap.

Table 2.5 Assembly procedures of the blade trap.

Procedure	Content
Checking	<p>Soak the blades in acetone bath for 30 minutes, soak the blades in ethanol bath for 5 minutes, as the blades are very important and fragile.</p> <p>Process the DC 820pF capacitors, soak them in acetone bath for 5 minutes, soak them in ethanol bath for 1 minute.</p> <p>Lean the blades against the beaker, otherwise it is not easy to be taken out when it sinks.</p> <p>The position of the DC capacitor is chosen to allow for clearance for the screws, as well as for the gold ribbon.</p> <p>The blades can be soaked in ethanol bath when not in use.</p>
Spot welding	<p>Process the gold ribbon by sonicating it with acetone for 30 minutes and with ethanol for 5 minutes.</p> <p>Cover the welding machine with aluminium foil before placing the blades to prevent them from scratching.</p>
Preparation	<p>Prepare hlders, PCBs, sapphire chips, indium foil, M2 and M1.5 screw sets, spanners.</p> <p>Make indium foil soaked in acetone bath for 30 minutes and in ethanol bath for 5 minutes, sonicate the rest with acetone for 30 minutes and with ethanol for 5 minutes.</p>
Assembly	<p>Apply indium foil to the sapphire piece, with the front of the indium foil flush with the top of the round hole to prevent short-circuiting the blade.</p> <p>Hold the blade parallel to the sapphire piece, remove the excess indium foil and fold the top of the gold ribbon</p> <p>Attach indium foil to the holder, then fix the sapphire piece to it, fix the PCB board to the side of the holder and pass the gold ribbon through the air, leaving a certain length of gold ribbon to prevent it from melting when soldering, donnot block the light path.</p>

The connection of the blade electrodes is mainly done by means of gold ribbon (AME-TEK) and Kapton insulated wire (Accu-Glass Products). When selecting materials we need to be aware of ultra-high vacuum and cryogenic compatibility. Some of the circuit connections are made prior to assembly and the rest is done afterwards. Before assembling the blade, a 820 pF capacitor is fixed with silver epoxy between each DC electrode and ground on the two DC blades. The purpose of this capacitor is to create a low impedance between the DC electrodes and ground, reducing the voltage splitting of the RF signal on the DC electrodes. The gold ribbon is connected to the electrodes with the spot welder at one end and to the pads of the PCB with solder at the other. We will later connect the pads to the corresponding connections with Kapton insulated wire, where the DC electrode wires are connected to the corresponding wires from the DC feedthrough through the heat sink twice, and the two RF electrode wires are connected to the two wires at the output of the helical resonator.

## 2.4 Yb oven

In order to generate the atomic beams of Yb, we built two separate ovens from two stainless steel tubes, but integrated into a single feedthrough and both able to be used to load ions. The  $^{171}\text{Yb}$  oven has an abundance of 90% and The  $^{174}\text{Yb}$  oven has an abundance of 98%. As the Yb source is in block form, we need to cut it into small pieces and insert it into the stainless steel tube.



(a) Put all the components together.      (b) Connect to feedthrough.

Figure 2.9 Assembly of the Yb oven.

In order to achieve UHV compatibility we chose to use copper, stainless steel and Macor when machining the parts of the oven. Before assembly and testing, we cleaned all the parts inside the ultrasound machine using acetone and ethanol as solvents. All the parts were assembled according to the drawings and the copper wires on the feedthrough were

attached to the stainless steel base, which was all screwed in place. We then used a spot welder and welded the stainless steel tube to the stainless steel wire, and the stainless steel wire to the stainless steel base, respectively. As the stainless steel tube has the smallest cross-sectional area, the highest resistance in the whole circuit is at the stainless steel tube, about  $0.5 \Omega$ , so the temperature is highest here too. I would recommend having some extra spare parts and testing the parameters of the spot welder in advance, as the stainless steel tube can easily break under unsuitable parameters. Finally the two Yb sources are filled into the corresponding stainless steel tubes.

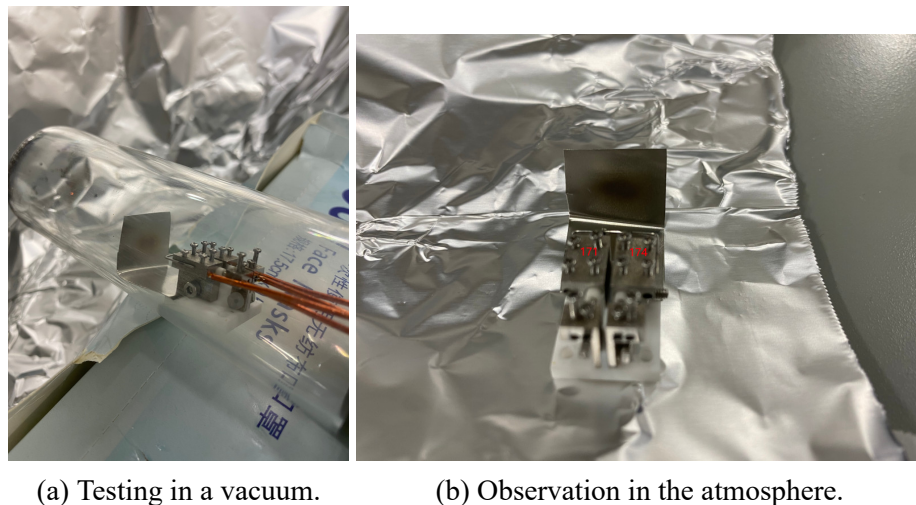


Figure 2.10 Testing of the Yb oven.

Each oven is mounted in such a way that the outgoing atomic beam is directed towards the trapping area. The oven feedthrough replaces an 1 inch window in the axial direction of the trap. the glass in the corresponding position of the 40 K shield and 4 K shield is also replaced with a round aluminium plate, the centre of which is a square hole with a 5mm side to pass through the Yb flux. As the cryostat has assembly errors, I would recommend preparing round aluminium plates with different opening positions in advance. Ultimately we need to be able to see the trap through the opposite window, with the square hole and the oven in the same line.

Table 2.6 Parameter variation during Testing the Yb oven.

Oven	Initial vacuum	Ending vacuum	Threshold current
$^{171}\text{Yb}$ (Left)	$4.0 \times 10^{-6}$ mbar	$8.6 \times 10^{-6}$ mbar	4.2 A
$^{174}\text{Yb}$ (Right)	$2.3 \times 10^{-6}$ mbar	$6.5 \times 10^{-6}$ mbar	3.9 A

In the process of loading ions, when this stainless steel tube is heated resistively by an electric current, a spray of atomic Yb is produced. The temperature reached depends

on the current and the time of operation. If either of these two factors is too high or too long, this can lead to rapid evaporation of the Yb and thus the formation of a spray dense enough to cover its surface (e.g. ion trap electrodes or vacuum windows). To prevent this, each oven is tested in advance. A stainless steel sheet is placed in front of the oven and then the oven is placed in a transparent vacuum chamber and the vacuum is reduced to approximately  $4 \times 10^{-6}$  mbar using a turbo-molecular pump, so that a test system can be set up. We tested each oven in turn, starting at 0 A and increasing the current by 0.1 A every 10 seconds, observing the change in vacuum level and the colour of the stainless steel sheet. We can observe both the darkening of the stainless steel sheet and the rapid rise in pressure, at which point the current value is the threshold current for the corresponding oven.  $^{171}\text{Yb}$  oven has a threshold current of 4.2 A and  $^{174}\text{Yb}$  oven has a threshold current of 3.9A, but the current values we use in practice will be lower than this threshold, the exact values need to be measured in the corresponding experiments. The exact values need to be measured in corresponding experiments, such as observing the fluorescence of Yb atoms and loading Yb ion.

## 2.5 Optical and imaging system

Whether trapping ions or manipulating them, we need lasers. In our laboratory, tunable diode lasers (Toptica DL pro HP) are used widely, mainly because these products are very well mature. For ion trap systems, a stable light source is very important. Experimentally, we need these lasers to be switched on and off quickly, typically in a few hundred nanoseconds. It is also necessary that these lasers can be stabilised over long periods of time and that these laser controllers have stable software systems. Laser stabilisation covers mode, frequency, power and polarisation. Typical laser stabilisation lasts from a few hours to a day, including laser frequency locking. This is sufficient for our trapped ion experiments, but longer stabilisation times are preferable. In the experiments, these stable lasers are used for: ion loading, Doppler cooling, optical pumping, state detection, repumping and sympathetic cooling. In addition to the laser light path into the cavity, I also built an imaging system to collect the fluorescence emitted by the ions, enabling real-time observation and state detection of the ions.

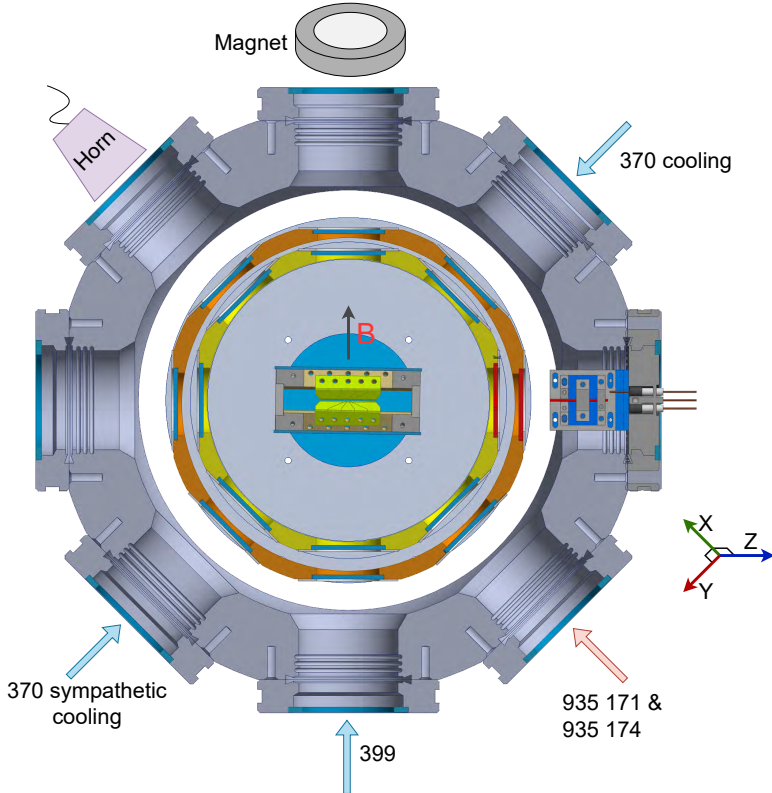


Figure 2.11 Optical layout of the ion trap and the vacuum chamber.

### 2.5.1 Laser sources and power allocation

The light sources in the laboratory are placed on several separate optical tables. Since the principles of the optical path setup are similar, we can present the light sources and power allocation in a common way, as shown in Fig 2.12. The cryogenic trap platform requires a 370 nm laser (L1), a 399 nm laser (L2) and two 935 nm lasers (L3, L4). The two 935 nm lasers are shared with other ion trap platforms in the lab, one for trapping  $^{171}\text{Yb}^+$  ions and the other for trapping  $^{174}\text{Yb}^+$  ions. The 399 nm laser is used for loading ions. Depending on the type of ion to be loaded,  $^{171}\text{Yb}^+$  or  $^{174}\text{Yb}^+$ , we can change the wavelength of the 399 nm laser. This 399 nm laser is also shared with other trapped ion platforms in the lab and only one 399 nm laser is needed. Since loading ions is not very frequent and most of the time we need to load  $^{171}\text{Yb}^+$  ions, and modifying the wavelength of the 399 nm laser will not affect the stable trapping of the loaded ions.

The output power of a semiconductor laser is approximately 10 mW, depending on the wavelength and model, the laser output power may vary a little. The output power of the 370 nm laser (L1) is 13 mW, other lasers have similar output power.

As the nominal light output from the laser is linearly polarised, a power attenuation unit was formed using a half-wave plate(HWP) and polarization beam splitter(PBS )to

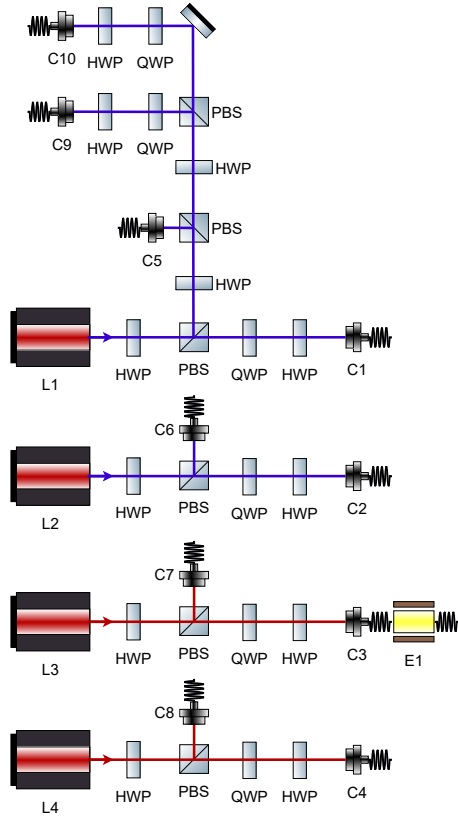


Figure 2.12 Optical path of laser power allocation.

split the laser output into two parts, which are separately coupled into the fibre. Each fibre will act as the light source for the next stage of the optical path, thus making the optical path a modular one. Each laser has one optical fibre connected to the wavemeter (C5, C6, C7, C8). Because polarisation stabilisation is not required, a single-mode fibre is used, with a typical power of approximately  $50 \mu\text{W}$ . The other fibres are the light sources for the rear optical paths (C1, C2, C3, C4) and require high power, typically  $5 \text{ mW}$ . At the same time their polarisation needs to be stable over time and we use single-mode polarization-maintaining fibres. In order to adjust the polarisation direction to match that of the single-mode polarization-maintaining fibre, we use a polarisation adjustment unit consisting of a HWP and quarter-wave plate(QWP). We need to maximize the efficiency of the fiber coupling, which requires a good laser output mode and good mode matching, which can be done with a lens pair, I don't show this in the diagram.

The 370 nm laser also has two splits: one (C9) is connected to the optical cavity for narrow linewidth frequency locking of the laser, and the other (C10) is set aside.  $^{171}\text{Yb}^+$  repumping beam requires 3.0695 GHz sidebands, so the 935 nm laser (L3) has a fibre EOM (E1) in the rear optical path.

Table 2.7 Wavelengths of lasers in the laboratory corresponding to loading different isotopes.

Isotope	370 Laser (nm)	399 Laser (nm)	935 Laser (nm)
$^{171}\text{Yb}^+$	369.526334	398.911150	935.188
$^{174}\text{Yb}^+$	369.525228	398.911570	935.180

## 2.5.2 Laser frequency stabilization

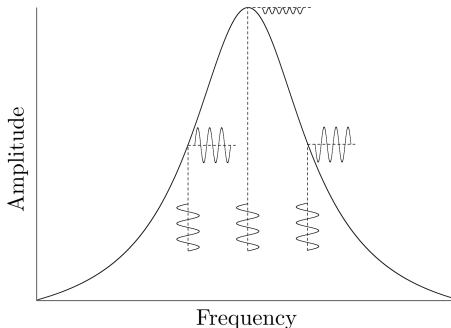


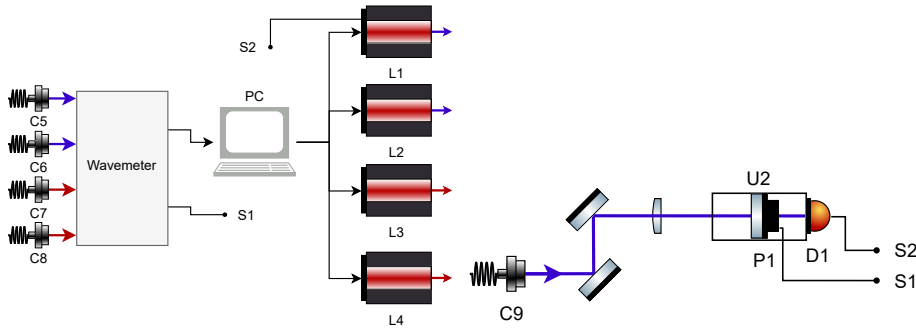
Figure 2.13 Illustration of simple frequency modulation for optical cavity.

The target linewidth of the laser frequency locking determines the laser frequency locking scheme. In my experiments there is no need for ultra-narrow linewidth laser locking, so the laser locking scheme is relatively simple and I have mainly optimised the automatic control of the frequency locking process. The measurement and locking of the laser frequency can be achieved with a wavelength meter, which has a relatively low bandwidth of about 10 Hz because the sum of the measurement time of the multi-channel wavelength meter and the computer readout time is about 100 ms, as shown in Fig 2.14(a). The standard deviation of the output frequency of the laser locked with this scheme is about 1 MHz, which meets my needs with a 399 nm laser and two 935 nm lasers, or if only to trap a small amount of ions then also my requirements for a 370 nm laser. The outgoing light from the laser is transmitted by optical fibres (C5, C6, C7, C8) to the input of the wavemeter, which is programmed to read the frequency on our PC and then programmed to adjust the voltage signal from the laser controller, thus creating a closed loop that locks the laser frequency. The wavemeter's measurements are affected by the environment, mainly air pressure and temperature. Therefore this frequency locking scheme will cause the locked laser frequency to be inaccurate due to inaccurate measurements, but this error is slow and periodic over time. So for 399 nm laser and 935 nm lasers we don't take this into account. I only calibrate the 370 nm laser once in 1 hour or longer, by measuring the resonant frequency of the  $\text{Yb}^+$  ion and feeding it back to the wavemeter's lock point. It would be possible to automatically calibrate the wavemeter for measurement errors if the

## CHAPTER 2 EXPERIMENTAL SETUP

---

wavemeter had a locked reference light all the way through, such as a 780 nm laser, but we have not done this because it is not necessary. The implementation of an automatic frequency lock is necessary as it will simplify the steps of daily operation. By laboratory standards these lasers need to be switched off when they are not in use, for example every night. I will adjust the operating parameters of the laser so that the laser mode can be stabilised back to a specific frequency range for approximately 10 minutes after each switch-on operation, which requires us to find a stable operating parameter for the laser. We then only need to program to communicate with the laser and the wavemeter to achieve automatic laser control and frequency locking.



(a) Optical path of the wavelength meter. (b) Optical path of the optical cavity.

Figure 2.14 Optical layout of laser frequency stabilization system.



Figure 2.15 Demodulated signal of the optical cavity photo diode.

The results of targeting the 370 nm laser with a wavemeter are not good enough because the feedback speed is too slow. We can increase the feedback speed with the assistance of an optical cavity, as shown in Fig 2.14(b), which reduces the standard deviation of the output frequency of the 370 nm laser to 300 kHz. I built this optical path on a breadboard in which an optical cavity (U2; SA200-3B, Thorlabs) was placed. The

outgoing light from the 370 nm laser (C9) is incident to the optical cavity. mode matching of the optical cavity is achieved by a pair of reflectors and lenses. Locking the 370 nm laser to the optical cavity is achieved by feeding the output signal of the photodiode (D1) back to the voltage signal of the 370 nm laser controller. In order to have the lock point at the point of maximum transmission light intensity of the optical cavity, I added a modulation signal to the current signal of the 370 nm laser and demodulated the signal from the photodiode (D1). This solution uses a simple optical cavity to increase the bandwidth of the laser locking. This scheme uses a simple optical cavity to increase the bandwidth of the laser locking. However, because environmental factors can cause the cavity length of the optical cavity to change, the locked frequency will change rapidly as the cavity length changes. I connected the voltage signal (S1) from the wavemeter output to the piezoelectric ceramic (P1) of the optical cavity, thus achieving a locking of the optical cavity length to the wavemeter.

### 2.5.3 Laser modulation

Making the laser modulation a separate module allows for modularisation of the optical path, which facilitates maintenance and testing, and also reduces the size of the optical path into the cavity, which in turn reduces the area of the breadboard where the cryogenic trap vacuum chamber is located. Optical layout of laser frequency stabilization system is shown in Fig 2.16. The main source of laser leakage during laser modulation is the higher order modes of the laser and stray light from the crystal during modulation. Adding a stage of fibre coupling can act as a spatial filter and help reduce leakage.

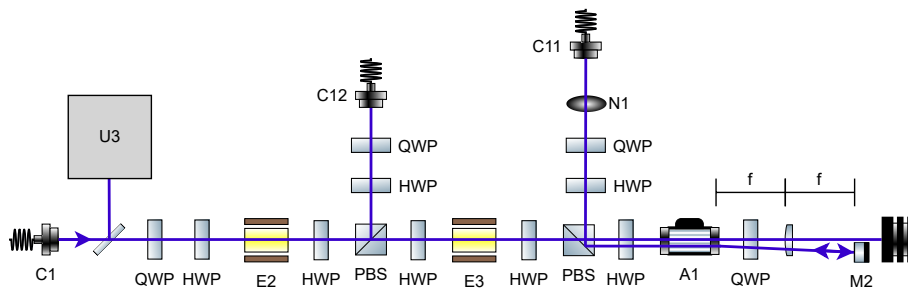
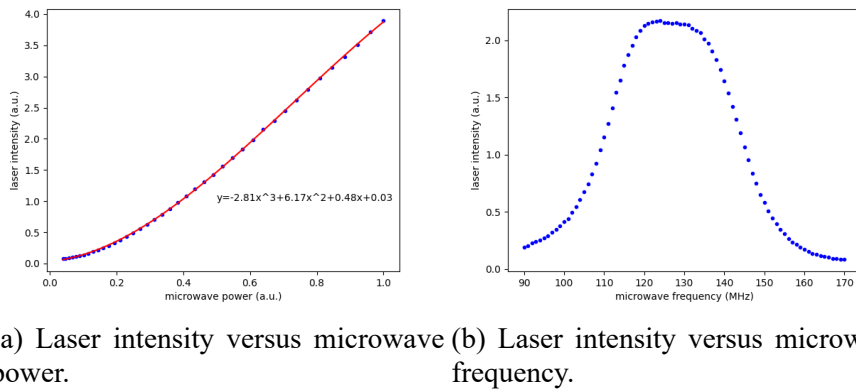


Figure 2.16 Optical layout of laser modulation system.

Experimentally, I need to add sidebands to the 370 nm laser, the 14.7 GHz sideband (E2) for Doppler cooling and the 2.105 GHz sideband (E3) for optical pumping. the electro-optic modulator (EOM) can implement these features. The frequency and modulation depth of the sidebands can be controlled by controlling the frequency and amplitude of the EOM input microwave signal. In addition, I need to control the frequency shift

and power of the 370 nm laser. This is because the difference in frequency required for Doppler cooling and state detection is approximately 12 MHz, and the frequency variation measured during calibration of the system can be compensated for by adjusting the frequency shift of the 370 nm laser. The acousto-optic modulator (AOM) provides these features. By controlling the frequency and amplitude of the microwave signal input to the AOM (A1) the frequency of the laser shift and the laser power can be controlled. However, the AOM modulation efficiency is affected by the microwave signal, as shown in Fig 2.17, and we need to compensate for this using software control during experimental operation.



(a) Laser intensity versus microwave power. (b) Laser intensity versus microwave frequency.

Figure 2.17 AOM modulation efficiency influenced by microwave signal.

The light source from the 370 nm laser is fed to the laser modulation module via a single-mode polarization-maintaining fibre (C1), which is reflected by a beam sampling mirror and enters the laser monitoring module (U3). A number of signal acquisition modules are integrated into the laser monitoring module to help me monitor the quality of the light source over time, including measurements of power, polarisation, laser mode and others. The main light source is modulated by two cascaded EOMs, the modulation depth of which can be maximised by adjusting the HWP. Part of the laser is coupled into the fibre (C12), which is then used for sympathetic cooling. To achieve the frequency shift, I built a double-pass configuration based on a 4f optical system, where the PBS serves to separate the incident light from the returned light by  $90^\circ$ , adjusting the HWP at the front to maximise the efficiency of the incident light and the HWP at the back to maximise the efficiency of the diffraction from the AOM. When the laser passes through the AOM, 0 order light is discarded and +1 order light is returned to the AOM by a 4f optical system consisting of a lens and a D-shaped pickoff mirror. The +1 order beam from the reflected beam passes through the QWP twice and is then reflected by the PBS into the fibre (C11),

this light is then used for global cooling, pumping and detection. There is a mechanical shutter (N1) in front of the fibre, which serves to completely shut off the light and reduce leakage.

#### 2.5.4 Optical layout of the cryostat breadboard

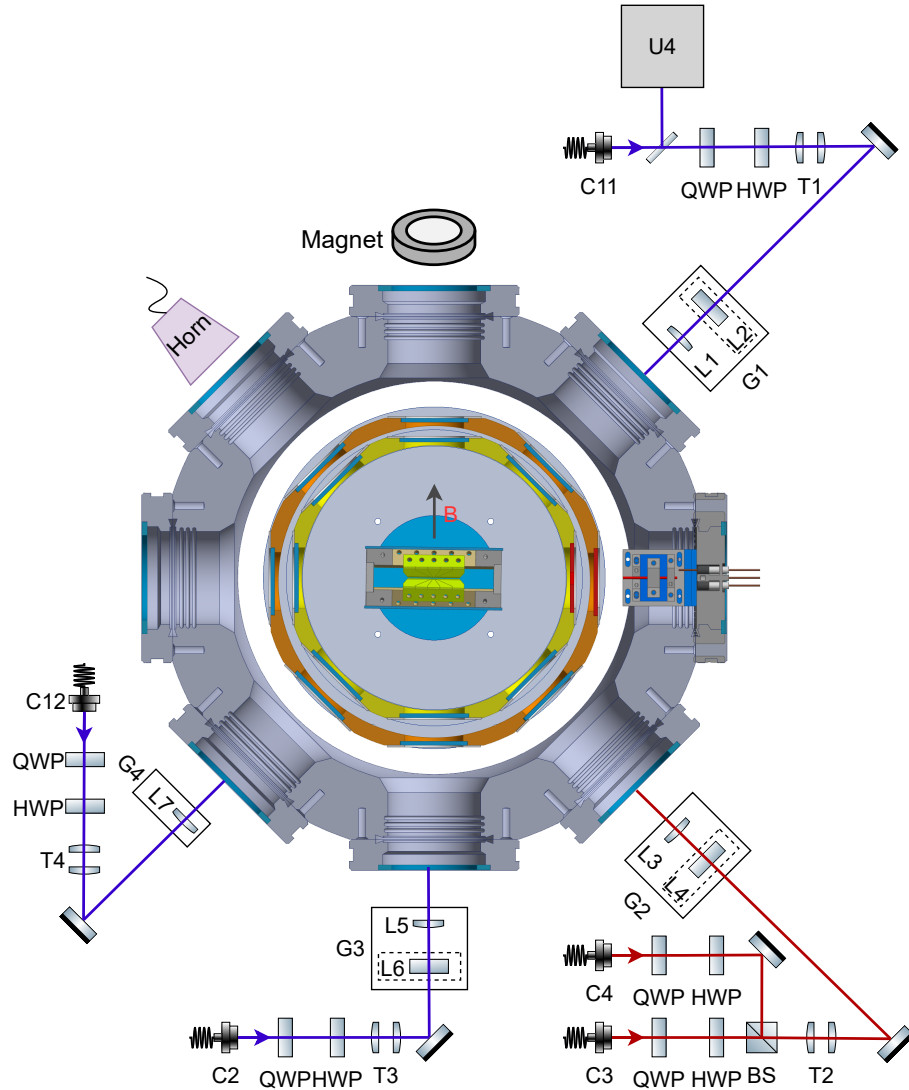


Figure 2.18 Optical layout of the cryostat breadboard.

Due to the large base area of the cryostat, the area left for the optical path on the breadboard is relatively small. The main function of the optical path built on the breadboard of the cryostat is to shape the beam into a specific shape and then inject it into the cavity. There are four windows on the Cryostat that are used to inject the laser. The laser light exiting the fibre collimator (C2, C3, C4, C11, C12) is first polarised by the QWP and HWP and then expanded by the lens pairs (T1, T2, T3, T4) to a suitable spot size, typically with a Gaussian diameter of approximately 10 mm. It is then incident on a long-

focus lens (L1, L3, L5, L7) into the cavity and forms a small spot in the centre of the trap, typically with a Gaussian diameter of about  $20\ \mu\text{m}$ . The long-focus lenses are mounted on a 3-axis linear stage (G1, G2, G3, G4; M-461-XYZ-M, Newport) with a Picomotor actuator (8301NF, Newport) in each axis of the stage to achieve high precision control of the beam position. Reducing the spot diameter at the trap is necessary to increase the power density, reduce stray light and improve the signal to noise ratio. It also helps me to monitor the displacement of the spot relative to the ions over time, which helps me to find unstable components or modules in the system at the beginning of the construction of the system. But when the length of the ion chain in the trap increases, I need some light spots to expand in the horizontal direction to about  $500\ \mu\text{m}$  in diameter. It is advantageous to be able to easily adjust the spot diameter in the horizontal direction. I added cylindrical lenses (L2, L4, L6) to the optical path where I needed to adjust the horizontal diameter, and by artificially introducing astigmatism, I was able to shift the horizontal focal position along the optical axis. A long-focused cylindrical lens with a focal length of approximately 1000 mm is generally used, mounted on a rotatable lens mount so that the tilt angle of the elliptical spot can be adjusted and the cylindrical lens can be removed when the elliptical spot is not required.

The stability of the 370 nm laser (C11) is so important to the experiment that a laser monitoring module (U4) has been installed at the outgoing point of the fiber. This light is global light and is required for ion loading, Doppler cooling, optical pumping, and state detection. In order to trap both  $^{171}\text{Yb}^+$  and  $^{174}\text{Yb}^+$ , two 935 nm lasers (C3 and C4) were combined into the cavity and their function was rupumping. Combining these two 935 nm lasers at the front stage would have been a better option, but this was not done due to space planning in the laboratory. The 399 nm laser (C2) is used for ion loading and the 370 nm laser (C12) is used for sympathetic cooling.

A permanent magnet is placed in front of one window to generate a magnetic field at the centre of the trap, approximately 5 Gauss, perpendicular to the direction of the ion chain. A horn is placed in front of one of the windows to apply microwaves.

## 2.6 Coherent microwaves

The system is outfitted with a microwave horn in order to coherently drive global spin rotations. The  $|\downarrow\rangle$  and  $|\uparrow\rangle$  states are directly coupled by a magnetic dipole moment, so the microwaves can directly drive rotations. Microwave signals are generated by mixing

---

CHAPTER 2 EXPERIMENTAL SETUP

Table 2.8 Measurement of microwave frequency and rabi rate.

Energy level	microwave frequency	$\pi$ -time
$ 1, 0\rangle$	200.0344 MHz	122.3
$ 1, -1\rangle$	188.0974 MHz	78.3
$ 1, 1\rangle$	211.9524 MHz	78.2

high frequency signals (Rohde & Schwarz SMB-100A, 11 dBm @ 12.4428 GHz) with low frequency signals (Analog Devices AD9910, around 200 MHz). The signals then passes through a high frequency amplifier and is output to a microwave speaker. Measurement of microwave frequency and rabi rate for different energy levels is shown in Table 2.8. Here the microwave frequency is added to 12.4428 Ghz to get the absolute energy level.

## CHAPTER 3 STABLE TRAPPING OF MULTIPLE IONS

For a newly built cryogenic trap system, the experimental implementation of stable trapping of multiple ions may take most of the project time before some quantum computing or quantum simulation experiments can be carried out. Experimental implementation of stable trapping of multiple ions involves not only achieving long-lived ion crystals, but also testing a stable standard experimental flow, debugging the experimental platform for various sources of noise, and developing an automatic experimental control system. From a project perspective, it is also a good idea to iterate and optimise the system while achieving stable trapping of multiple ions, and then try to solve the problem when the experiment gets stuck somewhere. Personally, I think more attention should be paid to experimental implementation of stable trapping of multiple ions, because for complex systems, the duplication of effort involved in finding a problem and then solving it can make the total time spent more than the time spent on building a stable experimental system in advance. However, the experimental implementation of stable trapping of multiple ions may not be well defined, and this may become a hole in the methodology.

### 3.1 Semi-automatic experimental control system

We usually divide the experimental tasks into daily operation tasks and current experiment tasks. The boundary between the two is not clear and we add some daily operation tasks by summarising some of the experimental tasks that have already been solved. Daily operation tasks can also be called experimental setup's parameters calibration tasks. For cryogenic trap systems, daily operation tasks also include the long-term monitoring of some system parameters. In an ideal laboratory environment it is possible to implement an automatic experimental control system, but in most laboratories we can only strive for a semi-automatic experimental control system. This is because some key points have to be controlled and checked by humans, mainly from some uncontrollable human disturbances.

Semi-automatic experimental control system mainly refers to the software system, which contains the front-end system, the back-end system, the database system and the experimental workflow.

The front-end system is the graphical interface that enables the experimenter to con-

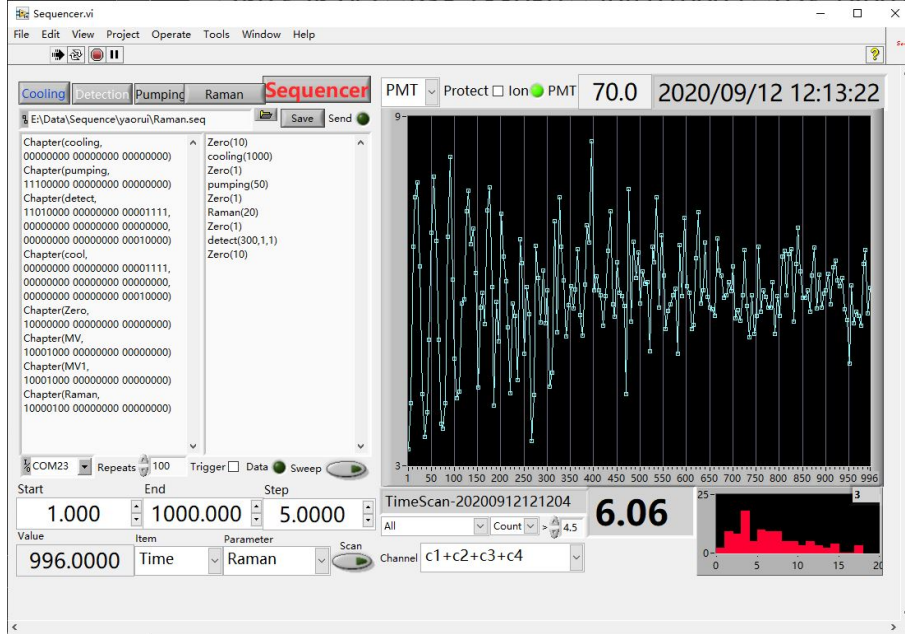


Figure 3.1 Labview front-end program (Sequencer).

duct experiments. The popular front-end technologies are client-side front-end technology and Web front-end technology. The more commonly used client-side front-end software in the laboratory are Labview, Mathematica, Matlab and other commercial software, which have rich functions and a friendly programming environment. I have written client-side front-end software based on python and pyqt5, as well as web front-end based on HTML5 technology in the course of my experiments. We can start building the experimental platform without focusing too much on front-end development, as these technologies are not necessary for physics research, and front-end technologies are rapidly growing, so it is possible to leave the front-end system to the professionals.

The back-end system is one of the core elements of the semi-automatic experimental control system. A unified back-end system will speed up the development of the entire semi-automatic experimental control system and facilitate communication and cooperation between project team members. We need the back-end system to control the experimental apparatus in a stable manner and in accordance with the experimental targets. There are a very large number of programming languages for developing back-end systems, suitable for use in the laboratory are C, python, etc. We can also consider using software that integrates front and back ends such as Labview, Mathematica, Matlab, etc. A good back-end system must adhere to lab safety rules, have a good logging system, have a good working state set, be stable over time and have a fast response time. If you are working with multiple people you need to consider version control and documentation

for development, such as code hosting. Long-term stability requires a good architecture, as instrument switches and new instrument additions occur frequently and the back-end system should not be offline too often. Instrument control protocols based on sockets and SCPI commands, mqtt protocol based instrument control protocols etc. can be considered. Fast response requires that the back-end program should have a response time of no more than 10-50 ms, which should be met in order to be able to perform complex operations.

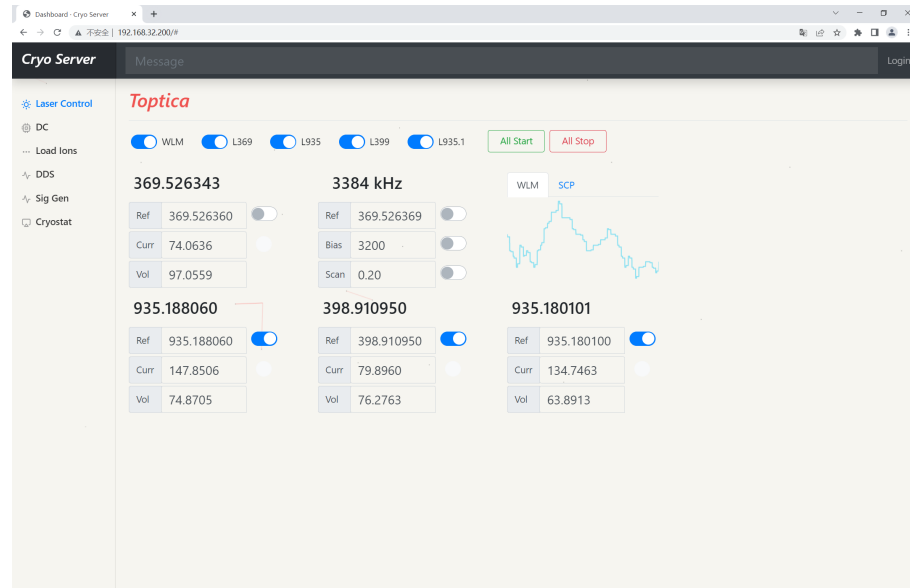


Figure 3.2 Web front-end program (Lasers etc.).

The database system has to take on the task of not only storing data but also taking into account data security. The database system on the experiment should take into account versatility and scalability, and should meet the needs of experimenters of different programming levels to use it. In addition to using SQL databases, InfluxDB, etc., it is also possible to use direct forms of experimental logs and file directory management, or even to use software such as excel directly for recording and management. In short, the database system should be compatible and easy to use as long as it exists and is standardised.

The experimental workflow does not primarily involve work on the code side of things. It is more like a framework bringing together the front-end system, the back-end system and the database system. We need to think about how to easily present the database and access historical data in the front-end system. We need to use it to log, deliver and present the results of experiments. We need to design daily operations and current experiments and easily code the corresponding tasks. Using Mathematica's notebook or using something like IPython based Jupyter will allow us to do this very well.

During the early build of the lab, we should implement scripted, semi-automated

tests under the command of an experimental workflow as soon as possible. With this layout, instead of focusing on front-end system development, we can focus on experimental workflow and database system refinement, while the back-end system can be updated with versioning to patch bugs and improve performance.

### 3.2 Monitor axial electrical potential drift

We often perform parameter calibration operation at trapping around 10 ions, but if current experimental tasks require ion number between 100 and 200, we need to perform parameter calibration at this ion number scale. This is because repeatedly changing the number of ions in a trap is an operation we do not want to perform. For a well-built blade trap, the upper limit of the ion number of 1D ion chains that can be stably trapped is fixed. When the ion spacing is close to the diffraction limit of the imaging system, we cannot obtain precise information on the ion position from the CCD and the crosstalk between the ions during state detection is too large for high fidelity state detection. In this case we increase the radial trap frequency by increasing the RF power and decrease the axial trap frequency by decreasing the DC voltage. However, there is an upper limit to this method of regulation. When the radial trap frequency is too high, RF heating will occur and the ion crystal will not be stable and will dissolve. In addition, when the ion chain length exceeds the width of the central electrode, we find an asymmetry in the imaging and structure of the ion chain. The asymmetry in the imaging of the ion chain is due to the aberration of the imaging system, we can optimise the imaging system to achieve a field of view of  $300 \mu\text{m}$ , but it may be more difficult to achieve  $600 \mu\text{m}$ . The asymmetry of the ion chain structure is due to the asymmetry of the blade electrode and the drift of the background electrical potential.

It is difficult to investigate what the source of the background electrical potential is, but it is objective and there may be more than one source. This phenomenon is clearly observed when we make the ion chain length exceed the width of the central electrode. When the DC voltage is set to a symmetrical value, the ion chain configuration tends to be asymmetrical. This asymmetry also changes over time, either after a day or after a month. It is inevitable that we will do something to the trap in the meantime. This asymmetry can be clearly observed if the oven current is raised to observe the fluorescence of the Yb flux, and the ions can be loaded without turning on the oven during at least one day. This asymmetry changes slowly if more than 200 ions are repeatedly loaded at a time over a

period of more than a week, which can be explained by the ions adhering to the surface of the blade after the crystal has been destroyed. We can compensate the background electrical potential with the DC voltage and produce the desired harmonic potential, but when the background electrical potential exceeds the range we can compensate for, we should find a way to eliminate the causes of the background electrical potential drift.

For a complex system, a restart operation is often an effective method. I will try to raise the temperature to room temperature or above 40 K. Over the course of several experiments I have observed that the background electrical potential is removed, which can be quantified by the maximum number of ions that can be stably trapped, or characterised by the asymmetry of the background electrical potential. However, I have occasionally observed that this restart operation does not work completely, and in general this restart operation is effective, but lacks sufficient quantitative data to generalise the factors and values that are truly effective.

### 3.3 Calculate axial electrical potential with 1D ion chains

We can calculate the axial electrical potential with 1D ion chains. we can use a CCD to measure the position of each ion in the 1D ion chains. this measurement is usually subject to error, and the error is different for different positions of the ions. For a chain of ions, the aberration is smaller for ions near the centre of the field of view and larger for ions near the edge of the field of view. If the ion chain exceeds the edge length of the CCD sensor, we can also measure the position of the ions in sections by moving the objective. In addition to the measurement error, the algorithm used to calculate the ion position can also produce a corresponding error. Commonly used algorithms for measuring ion positions are linear algorithms based on computer vision, which have the advantage of being fast and able to give results within 10ms. The other algorithm is a fitting-based algorithm, which is less fast and less convergent and is very dependent on the signal-to-noise ratio, but can achieve high accuracy with the right parameters. We can then use the algorithm to find the equilibrium position of the ion chain for a given number of ions and the electrical potential parameter as a calculated value. The difference between the measured and calculated values can then be fed back to the electrical potential as a function of error, so that the parameter with the lowest error, i.e. the axial electrical potential at this point, can be iteratively found.

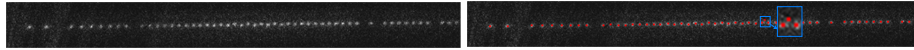
Fig 3.3(a) shows the use of Mathematica's code to identify a typical ion chain image.

```

IonPositionReadOutWithSpecialParameter[im_] :=
Module[{filteredImage, edgeofImage, m, centerPosition, component},
|模块
edgeofImage = EdgeDetect[im, 2.5`, 0.052`, Method -> "Canny"];
|边缘检测 |方法
m = MorphologicalComponents[edgeofImage] // Colorize;
|形态学分量 |着色
component = ComponentMeasurements[m, {"Centroid", "FilledCircularity"}];
|分量度量
centerPosition = Table[component[[i, 2, 1]], {i, 1, component // Length}]
|表格 |长度

```

(a) Mathematica code.



(b) Raw image.

(c) Image after processing.

Figure 3.3 Usage of Mathematica's code to identify a typical ion chain image

Fig 3.3(b) and Fig 3.3(c) show the original image and the processed image respectively, with the red dots representing the centre of the identified ions. The background scattered light and the aberration of the image can have an effect on the result of the identification. As can be seen from the recognition results in the blue box in Fig 3.3(c), the trailing of a particular ion may be determined as a new ion, but the conformation of the ion chain precludes this possibility. Optimising the algorithm may be a good idea, but the noise introduced by the imaging system will not be eliminated. Even if the recognition algorithm is optimised using criteria such as no jump in neighbouring ion spacing, ion chain linearity judgement, etc., the noise will still reduce detection fidelity during state detection, and the benefit of reducing noise by optimising the imaging system is much greater. Fig 3.4 shows code using python to recognise an image of a long ion chain. The algorithms used are similar, so are prone to recognition errors for larger ion chains.

Now that we are able to obtain information on the location of the ions, we next use a ingenious algorithm proposed by Yukai Wu to calculate the axial electrical potential. The idea of the fitting is very simple. For given trapping potential, we can compute the equilibrium positions of the ions. Then we can adjust the trapping potential to get a best fit of the measured ion positions. For this purpose, it is desired to use a discrete set of parameters to describe the trapping potential. For example, here we use the Legendre polynomials. To get better convergence properties, we scale the axial positions to about  $[-1, 1]$ , which can be recovered in the end.

In Fig 3.5 we present the fitting results for various ion numbers under the same settings of potentials and the CCD camera. Fitting results for (a, b)  $N = 6$ , (c, d)  $N = 9$ , (e, f)  $N = 13$ , (g, h)  $N = 19$ . The fitting of the trapping potential uses up to 2nd order

```

def CVIONS_FAST(image, LoG_sigma=1.5, threshold=0.3):
    # some computer vision algorithms
    image_log = gaussian_laplace(image, LoG_sigma)
    image_log = 1 - (image_log - np.min(image_log)) / (np.max(image_log) - np.min(image_log))
    image_bn = np.where(image_log > threshold, 1, 0)
    image_lb = label(image_bn)
    # label ions
    lb_num = np.max(image_lb)
    para_num = 4
    para_cv = np.zeros((lb_num, para_num))
    for lb in range(1, lb_num + 1):
        count = image[image_lb == lb]
        wgt = count / np.sum(count)
        y, x = np.where(image_lb == lb)
        max_count = np.max(count)
        x0 = np.average(x, weights=wgt)
        y0 = np.average(y, weights=wgt)
        s = np.count_nonzero(image_lb == lb)
        para_cv[lb - 1, :] = [max_count, x0, y0, s]
    # calculate ion positions
    order = np.argsort(para_cv[:, 1])
    for i in range(para_num):
        para_cv[:, i] = para_cv[order, i]
    return para_cv

```

(a) Python code.



(b) Image of 245 ions.

Figure 3.4 Usage of Python code to calculate 245 ions' position.

polynomials(a, c, e, g) and up to 4th order polynomials (b, d, f, h). The blue and red dots are the measured positions and the fitted ones, respectively. The fitted data are lifted in the vertical direction to better distinguish the two sets of data. The green curves are the fitted axial trap potential. As we can see, 2nd order polynomials do not give good fitting results, but polynomials up to 4th order generally fit well.

Furthermore, we can see in Fig 3.6 that the fitted potentials for different ion numbers agree well with each other, apart from a constant shift which is not relevant to the equilibrium positions and has been removed. Fitted trapping potential for  $N = 6$  (red),  $N = 9$  (green),  $N = 13$  (orange) and  $N = 19$  (blue) ions.

Finally, we comment that the method can be applied to the case where dark ions exist, so long as we can identify the order of the bright and the dark ions. Then we simply use the positions of the bright ones in simulation to fit the trapping potential. As shown in Fig 3.7, the fitting results is almost the same if the number of dark ions is not too large. The fitting results for the  $N = 19$  case in Fig 3.5 with the ion 6 and ion 9 chosen as dark ions. The fitted potential (green) almost overlaps with the previous one (black) where all the ions are bright.

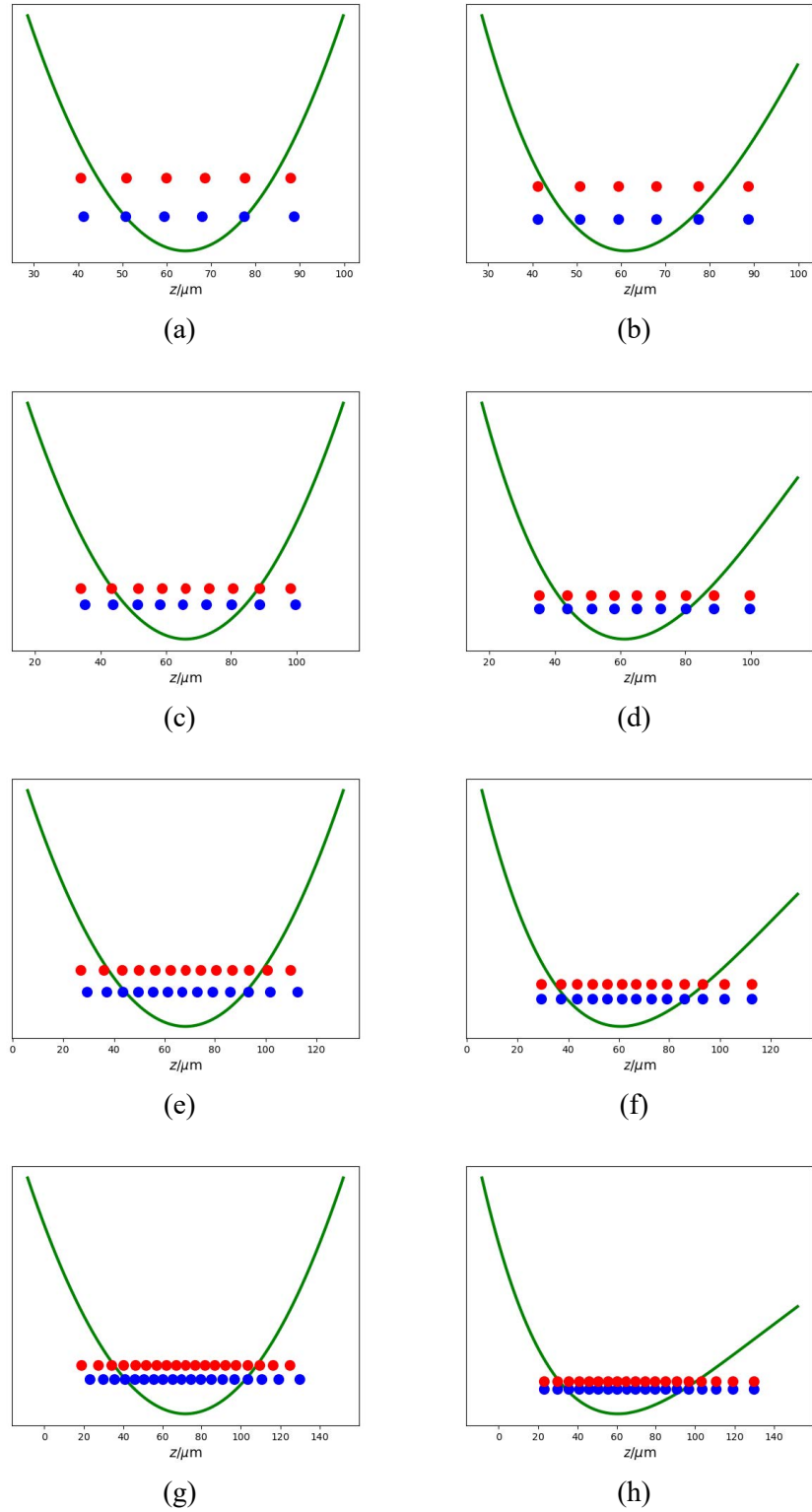


Figure 3.5 Fitting results for various ion numbers.

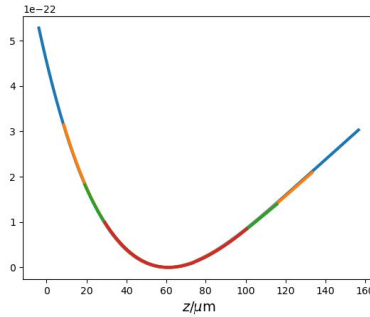


Figure 3.6 Fitted trapping potential for different ion number.

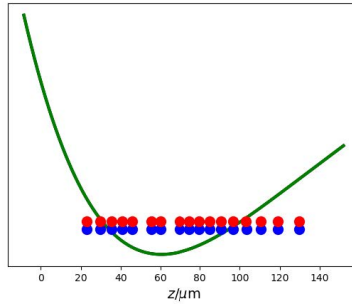


Figure 3.7 Fitted trapping potential with dark ions.

### 3.4 Fitting the electrical potential coefficient for each electrode

For a fixed electrical potential, we can capture different numbers of ions, as shown in Fig 3.8, 2, 12, 24, 34, 42. For each image, we can calculate the position of the ion and fit it to the electrical potential at that time. Red circles and dots on the right-hand side indicate the calculated position of the ion and the equilibrium position of the ion at the fitted electrical potential, respectively. The black dots indicate the presence of dark ions. The electrical potential can be expressed as

$$\phi_n(x) = \sum_{i=1}^n \alpha_i P_i(x), x = z/l_0, \quad (3.1)$$

where  $z$  is the true position of the ion,  $l_0$  is half the length of the ion chain,  $P_i(x)$  is the Legendre polynomial of degree  $i$  and  $\alpha_i$  is the coefficient of the expansion.

Since the electrical potential has not changed, the fit should be consistent for different numbers of ions. As shown in Table 3.1, the coefficients of the Legendre polynomial have consistent convergence for data with 2 to 42 ions.

If we were to use this algorithm directly to calculate the coefficients of the electrical potential at different voltages, we would end up with scattered results due to overfitting.

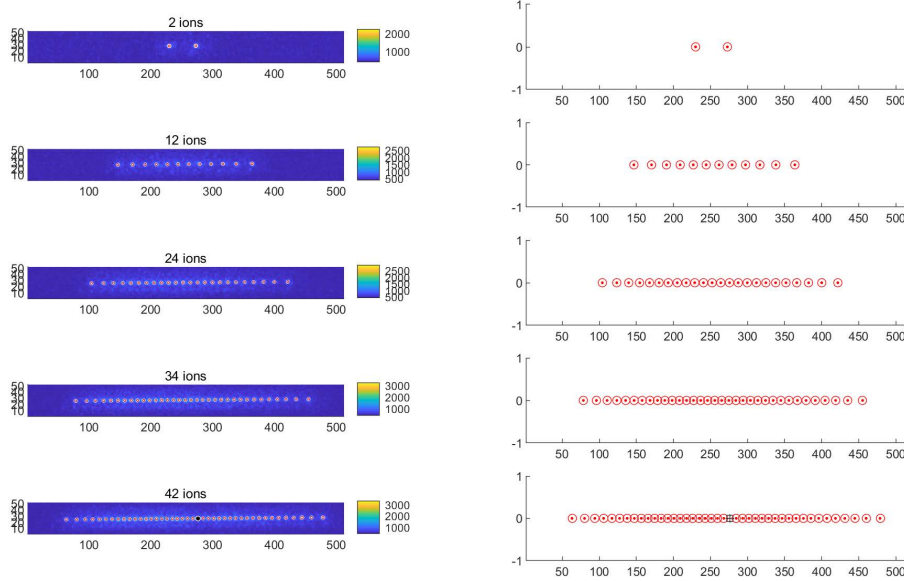


Figure 3.8 Fit trapping potential up to 42 ions.

Table 3.1 Fitting the electrical potential coefficient

Ion number	$\alpha_1$	$\alpha_2$	$\alpha_3$	$\alpha_4$
2	7.59183	212.463	0	0
12	12.5574	207.098	-45.04	40.0967
24	10.8866	204.913	-50.165	48.4474
34	10.8904	204.944	-49.784	48.0492
42	10.7205	205.988	-55.486	47.6406

So we need to assume that the coefficient of the electrical potential is fixed for each electrode and then decompose the electrical potential from the actual voltage into the sum of each electrode,

$$\alpha_i = \sum_{s=1}^5 \alpha_i^s U_s \quad (3.2)$$

where  $\alpha_i^s$  the coefficient of the electrical potential generated by each pair of DC electrodes,  $s$  is the order number of the electrodes, there are 5 pairs of electrodes in total. And  $U_s$  is the voltage applied to the electrodes.

I trapped 51 ions at a fixed electrical potential, as shown in Fig 3.9(a). Although the applied electrode voltage is symmetrical, the resulting potential field is asymmetrical, which is not what we want. I then added a fixed voltage to each pair of electrodes, at which point I could find the new electrical potential. The single result may have a large

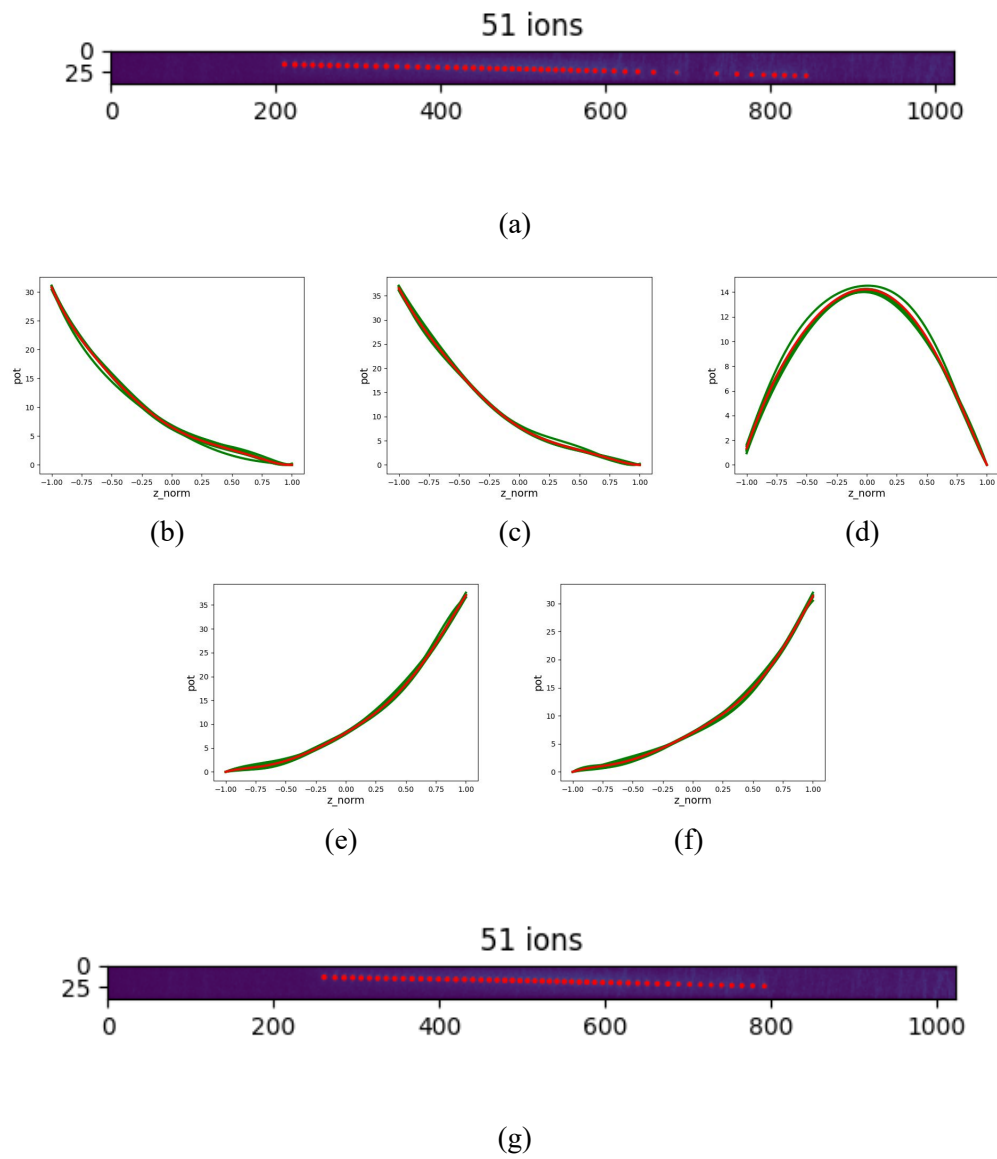


Figure 3.9 Fit the electrical potential coefficient for each electrode.

error, but if the voltage is increased in equal steps, it can be fitted to give  $\alpha_i^s$ . In Fig 3.9(b)-(f), I have plotted the electrical potential generated by the 5 pairs of electrodes. The green line represents the increase in electrical potential for equal steps of increasing voltage, and you can see that the increase in electrical potential is fixed. The red line represents the average of these data, and I think this value can represent the coefficient of electrical potential generated by each pair of DC electrodes. Next I calculated at what voltage settings this asymmetry could be compensated for and then achieved the result shown in Fig 3.9(g), where the ions are equally spaced.

### 3.5 Stabilization of axial electrical potential

When the number of ions becomes larger, we encounter some challenges. On the one hand the applicability of the algorithm can be problematic. For a quasi-1D chain of 126 ions as shown in Fig 3.10(a), the original algorithm fails due to the emergence of the zig-zag configuration. Since the original algorithm is only valid for 1D ion chains, we can consider optimisation algorithms to solve this problem. On the other hand, when experimental parameters such as image aberrations, adjustable range of voltages, etc. can gradually become a major source of noise, they can cause excessive errors or be too unstable, and we can solve this problem by refining the physical system.

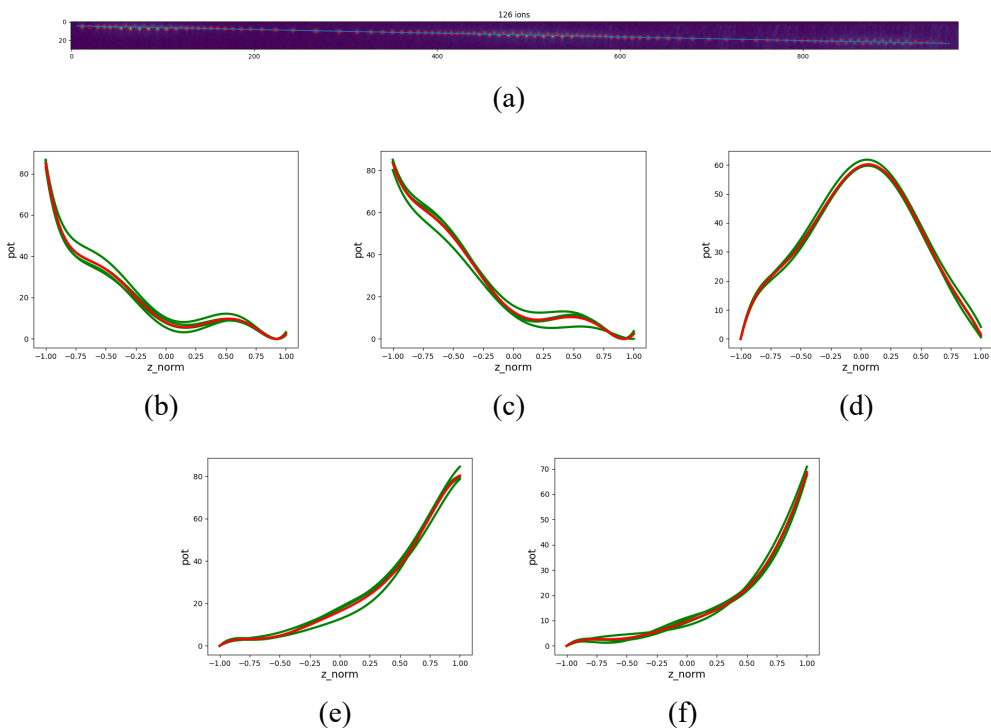


Figure 3.10 Fit the electrical potential coefficient with a 126-ions quasi-1D chain.

There are a number of ideas for optimisation algorithms, one simple idea is to abandon the calculation of the theoretical equilibrium position for a given electrical potential and take the equilibrium position of the ion directly from the image and invert the electrical potential at this point according to Coulomb's law. Using this method we can obtain the electrical potential for five pairs of electrodes as shown in Fig 3.10(b)-(f). It can be seen that at this scale of ion numbers the error becomes larger.

## 声 明

本人郑重声明：所呈交的学位论文，是本人在导师指导下，独立进行研究工作所取得的成果。尽我所知，除文中已经注明引用的内容外，本学位论文的研究成果不包含任何他人享有著作权的内容。对本论文所涉及的研究工作做出贡献的其他个人和集体，均已在文中以明确方式标明。

签 名： \_\_\_\_\_ 日 期： \_\_\_\_\_